

Vibrational similarities in jamming-unjamming of polycrystalline and disordered granular packings

Juan C. Petit,^{1,*} Saswati Ganguly,¹ and Matthias Sperl^{1,2}

¹*Institute of Materials Physics in Space, German Aerospace Center (DLR), 51170 Köln, Germany*

²*Institut für Theoretische Physik, Universität zu Köln, 50937 Köln, Germany*

(Dated: November 6, 2024)

Jammed structures with finite shear modulus emerge from polycrystalline monodisperse and disordered bidisperse granular packings. To link these macroscopic mechanical properties with microstructural characteristics, we examine the vibrational behavior of two-dimensional polycrystalline monodisperse and disordered bidisperse systems using discrete element method simulations. The vibrational density of states (DOS) reflects structural disorder and soft modes, and we analyze this for both types of packings as they approach jamming and unjamming densities. Our results reveal that the low-frequency plateau in the DOS, observed in both polycrystalline and disordered packings, originates from nonaffine particle displacements, particularly those involving “rattlers”, which are prominent near jamming and unjamming states. Although the jamming and unjamming process is irreversible, we find no evidence of expected history dependence in the DOS across any of the systems studied.

The phenomenon of jamming in granular media is critical for understanding the transition between fluid-like and solid-like states in granular packings [1–11]. This transition is not merely a theoretical concern; it has significant implications for practical applications across various fields, including material science, geophysics, industrial processes, and cell biology [12–19]. As granular systems undergo jamming, they acquire rigidity, a property traditionally associated with crystalline solids, which exhibit long-range order [20, 21]. However, disordered solids, which lack this long-range order, also resist external stresses, challenging our conventional understanding of rigidity and mechanical stability [22].

Previous theoretical research has explored the quantitative transition in mechanical behavior as 3D monodisperse crystalline structures evolve into disordered solids [9]. This study has identified intermediate packing states—highly ordered polycrystalline structures—that exhibit mechanical properties akin to disordered systems, particularly under low-pressure conditions near the jamming density. However, at high pressures, the mechanical response of these polycrystalline packings becomes comparable to that of crystalline systems. Similarly, two- and three-dimensional simulations reveal an order-disorder transition that demarcates crystalline solids from disordered ones [11]. In both 2D and 3D, this transition is marked by an intermediate phase where polycrystalline packings exhibit mechanical properties distinct from those of ordered crystals and fully disordered states. The vibrational density of states (DOS) for a 2D triangular crystal at a fixed packing fraction, ϕ , is significantly influenced by increasing disorder. As the disorder intensifies, the DOS shifts from a crystalline profile (low disorder) to a polycrystalline form (intermediate disorder) and ultimately to a fully disordered structure (high disorder).

These observations suggest that structural changes in packing are closely mirrored in the DOS, particularly at low frequencies, where soft modes—such as the boson peak—become prominent.

Although the impact of the disorder on the mechanical properties of polycrystalline and disordered packings is well-studied [3, 9–11], the evolution of their vibrational behavior during jamming and unjamming, and comparisons between these states, remain largely unexplored. A compression-decompression protocol can significantly alter the packing structure, thereby impacting the mechanical properties of the system [5, 23, 24]. These structural changes are expected to be directly reflected in the DOS, capturing the influence of packing modifications on vibrational modes and mechanical behavior. How does the vibrational behavior of the packing differ at jamming and unjamming states after these structural modifications? Most research focuses on either jamming or unjamming, often overlooking the interplay between the two. Comparing polycrystalline and disordered structures helps clarify whether the soft vibrational modes arise solely from disorder or if they also emerge in systems with partial order (polycrystals). This distinction offers deeper insights into the structural features that govern mechanical behavior. Our objective is to investigate how the vibrational behavior of two-dimensional (2D) polycrystalline monodisperse and disordered bidisperse packings evolves along the jamming and unjamming path, with a focus on how structural changes affect the corresponding DOS. 2D systems are easier to replicate in experimental setups, including microgravity, facilitating various empirical and fundamental studies that validate our theoretical perspective [25, 26]. Insights from simulations of compression and decompression during the jamming-unjamming transition in 2D granular solids can deepen our understanding of seismic wave propagation [25], acoustic wave behavior [27, 28], soil compaction, and granular flow in industrial applications [29, 30].

Simulations using the 2D discrete element method

* corresponding author: Juan.Petit@dlr.de

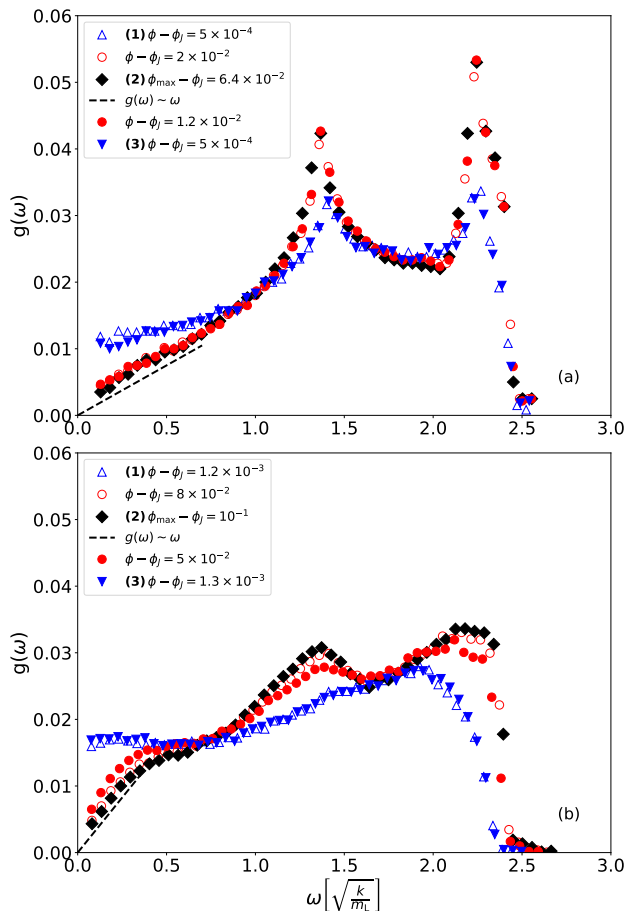


FIG. 1. The DOS for (a) monodisperse and (b) bidisperse packings along the compression-decompression process. Open red and blue (Δ , \circ) symbols represent the compression whereas solid red and blue (∇ , \circ) the decompression. $\phi_{\max} = 0.95$ is in black solid (\diamond). The Debye scaling law, $g(\omega) \sim \omega$, for solids is represented in black dashed lines.

are performed with the software MercuryDPM [31–33]. Monodisperse and bidisperse packings are formed by $N = 3000$ particles. The bidisperse packing has a number of large, N_L , and small, N_S , particles with radius r_L and r_S . The size ratio is $\delta = r_S/r_L = 0.73$ with a concentration of small particles of $X_S = N_S\delta^2/(N_L + N_S\delta^2) = 0.5$. Therefore, $\delta = 0$ represents the monodisperse packing. $\delta = 0.73$ and $X_S = 0.5$ are chosen to prevent long-range order [1, 2, 34]. Simulations are restricted to the isotropic compression-decompression protocol and the linear contact model without any friction between particles [33, 35, 36] (see Supplemental Material [37], Sec. I). Therefore, the compression-decompression process allows for extraction and analysis of the vibrational behavior of the packings from jamming to unjamming states.

Fig. 1 shows the DOS for monodisperse and bidisperse packings near jamming (1), at $\phi_{\max} = 0.95$ (2), and near unjamming (3), see the definition in [37], Sec. II.

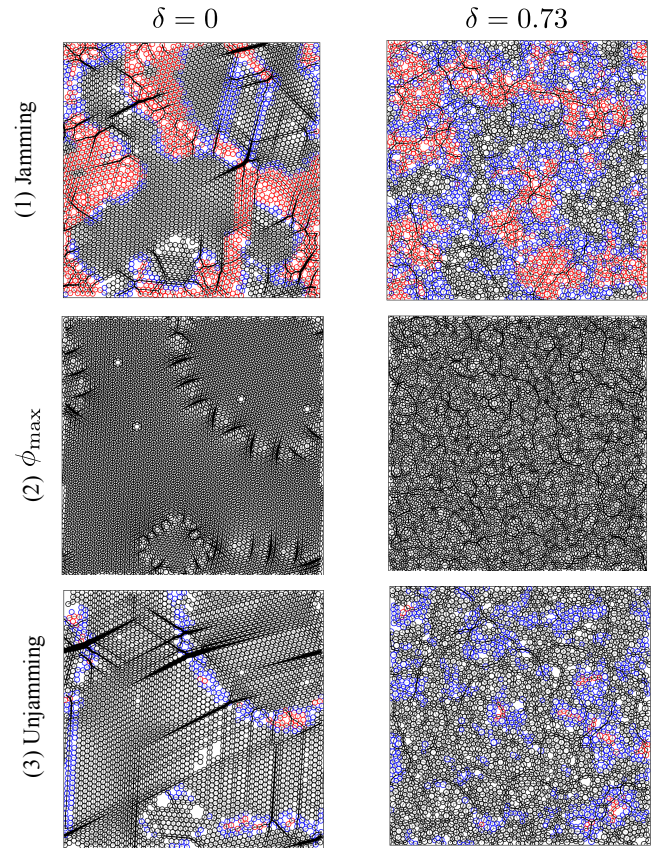


FIG. 2. Particle configurations and force chains for monodisperse ($\delta = 0$) and bidisperse ($\delta = 0.73$, $X_S = 0.5$) packings shown near jamming (1), ϕ_{\max} (2), and near unjamming states (3), consistent with Fig. 1. The width of the lines of the force chains are plotted accordingly to normal forces larger than $2\langle F_n \rangle$ to make the particle colors visible. The black, blue, and red circles represent the nonaffine motion of i th particle, corresponding to low $\chi_i < 1$, intermediate $1 \leq \chi_i < 5$ and high $\chi_i \geq 5$ values respectively.

Several intermediate cases are also included for comparison. During compression, typical van Hove singularities emerge at high frequencies near the jamming density in the monodisperse packing, as indicated by the open blue Δ in Fig. 1 (a). This observation aligns with the polycrystalline structure depicted in Fig. 2 (1). In the bidisperse system, such singularities do not exist due to the intrinsic disorder introduced by the different particle sizes, see Fig. 1 (b) and its corresponding configuration in Fig. 2 (1). With further compression, the van Hove singularities in the monodisperse case become more pronounced and broadened. Whereas in the bidisperse packing, two similar peaks appear at high ω . The more pronounced case can be seen at ϕ_{\max} in Fig. 1. These features indicate increased order after compression, as shown in Fig. 2 (2) and quantified using contact orientational order (COR) in Fig. 3. A key feature of the DOS near jamming is the plateau at low ω for bidisperse

packing, which is less pronounced in monodisperse packing. This is known as the boson peak, characterized by an excess of vibrational modes [2, 7–11]. The plateau at low ω in polycrystalline monodisperse packings suggests their vibrational properties resemble those of bidisperse disordered packing more than a single crystal structure, consistent with Ref. [9]. As the system undergoes further compression, the DOS evolves (open red \circ) and, at ϕ_{\max} (solid \diamond), follows the well-known Debye law at low ω (black dashed line). This behavior suggests that polycrystalline monodisperse and disordered bidisperse packings behave as continuum elastic mediums in certain limits. Therefore, the disordered bidisperse structure shifts from behaving like disordered solids at low compression to resembling crystalline solid behavior at high compression, see Fig. 1. This transformation is particularly pronounced at ϕ_{\max} , where the emergence of broader peaks, similar to those in the monodisperse case, suggests the development of some degree of local order. This observation is consistent with findings in 3D bidisperse packings, as noted in [23, 24, 38, 39], where local order appears at the jamming density and becomes increasingly prominent with further compression.

During decompression, the DOS for both systems evolves (solid \circ) like that observed during compression, once again displaying a plateau near the unjamming state (solid ∇). Interestingly, despite the variations in ϕ_J near the jamming and unjamming states of the monodisperse and bidisperse packings, the respective density of states remains remarkably similar at these points, as shown in Fig. 1. Even the intermediate DOS remains similar at comparable distances from the jamming/unjamming densities. A difference in the DOS is expected as the packing structure evolves during a complete cycle of compression and decompression. This structural change has been shown to affect the jamming density in previous work [5] and is evident in Fig. 3 (a)-(b), illustrating the fraction of particles in contact, $n = N^c/N$, as a function of relative packing fraction, $\hat{\phi}$. N^c is the number of particles in contact. $\hat{\phi}$ distinguishes between compression and decompression branches, with compression defined as $\hat{\phi} = \phi - \phi_{\max} \leq 0$ and decompression as $\hat{\phi} = \phi_{\max} - \phi > 0$. We observe that n increases with compression, showing a sharp transition at a specific $\hat{\phi}$ consistent with the jamming density. As $\hat{\phi} \rightarrow 0$, $n \rightarrow 1$, meaning all particles are in contact. During decompression, n drops discontinuously at a different $\hat{\phi}$ than at jamming, indicating the transition to an unjammed structure. The jamming/unjamming density, ϕ_J , is identified by a pronounced peak in the derivative of the particle number density, n , to ϕ . This peak at ϕ_J indicates a rapid shift in particle arrangement, marking the onset of either a jammed or unjammed structure, see Ref. [33]. The extracted jamming density for monodisperse packing is $\phi_J \approx 0.87$ whereas the unjamming is obtained at $\phi_J \approx 0.88$. The latter ϕ_J is consistent with the formation of some crystallization inside the packing but far

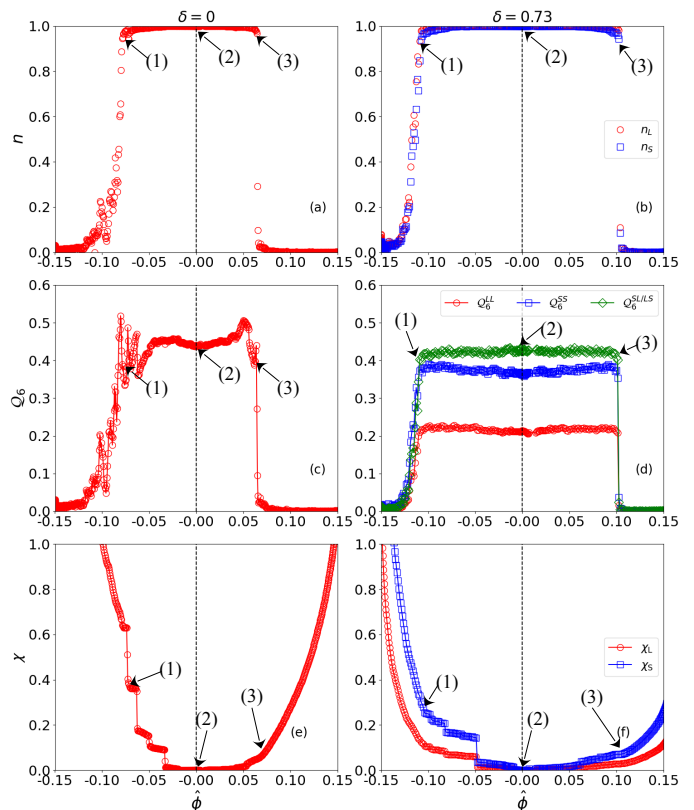


FIG. 3. (Top) Fraction of particles in contact, n , (Middle) contact orientational order, Q_6 , and (Bottom) the cumulative nonaffine parameter, \mathcal{X} , as a function of $\hat{\phi}$ for monodisperse (left panel) and bidisperse packings (right panel) with $\delta = 0.73$ and $X_S = 0.5$. \mathcal{X} is intentionally scaled by 1000 to enhance the readability of the y-axis. The arrows indicate (1) near jamming, (2) ϕ_{\max} , and (3) near unjamming. Particle configurations on these states are shown in Fig. 2. The dashed line corresponds to $\hat{\phi} = 0$ or $\phi = \phi_{\max}$.

from the triangular lattice structure of ~ 0.90 observed in Ref. [3]. Polycrystals are already formed near the jamming density (1), remain intact at ϕ_{\max} (2) after particle rearrangement during further compression, and persist even near the unjamming state (3), see Fig. 2. For the bidisperse packing, the unjamming density is $\phi_J \approx 0.84$, which is 0.5% higher than the jamming density. This value agrees with that reported for amorphous bidisperse mixtures in Refs. [3, 6]. The structure at jamming for bidisperse packings look disordered, confirmed by the homogeneous distribution of the force chains and more clearly at ϕ_{\max} , see Fig. 2. Such a structure evolves with minimal changes along compression-decompression paths. Subtle structural changes in both packings during this process are also supported by the structure factors presented in Sec. III of the Supplemental Material [37].

To better understand the changes in packing structure, we calculate the contact orientational order (COR), Q_6 , as a parameter quantifying the formation of potential six-fold lattice structures (see Sec. IV in [37]). This variable

avoids the ambiguities of the bond orientational order (BOR) and is more sensitive to sudden changes in contact numbers or other structural features compared to the structure factor, see Ref. [38]. Figs. 3 (c)-(d) display the evolution of \mathcal{Q}_6 for monodisperse and bidisperse packings. Monodisperse packings exhibit variations in \mathcal{Q}_6 after jamming due to particle rearrangement, stabilizing under further compression, see Figs. 3 (c). Notably, \mathcal{Q}_6 at ϕ_{\max} remains below 1, indicating that the system is not fully ordered and deviates significantly from the ideal value of $\mathcal{Q}_6 = 1$ expected for perfect hexagonal packing [11]. During decompression, \mathcal{Q}_6 slightly increases, suggesting some organization due to stored energy, before dropping at unjamming (see Fig. 2). For bidisperse packings, we quantify local structures between Large-Large (LL), Small-Small (SS), and Small-Large (SL) particles. Fig. 3 (d) shows that mixed contacts dominate the structure that evolves constantly, followed by small and large particle contacts that are slightly reduced near $\hat{\phi} = 0$. The latter is because particles with the same size slightly overlap at ϕ_{\max} , which tends to distort and induce disorder in the packing. Interestingly, all partial \mathcal{Q}_6 values at jamming (1) and unjamming (3) are identical, see the arrows in Fig. 3 (d). This suggests that the packing structure of the bidisperse mixture evolves with compression, while local configurations are restored upon decompression. This indicates that the configurations at jamming and unjamming are structurally similar. In contrast, identifying jamming and unjamming configurations for monodisperse packings in Fig. 3 (c) is more challenging. However, the arrows in panels (1)-(3) indicate similar local values of \mathcal{Q}_6 , consistent with the structure factor shown in [37]. Therefore, the preserved packing structure in monodisperse and bidisperse packings near jamming and unjamming likely indicates comparable vibrational and mechanical behavior in these states.

The similarity in local configurations at jamming and unjamming can also be analyzed by quantifying the nonaffine motion of particles during compression-decompression and examining its relationship with the plateau shown in Fig. 1. Figs. 3 (e)-(f) show the evolution of the cumulative nonaffine displacements, \mathcal{X} , as a function of $\hat{\phi}$ (see Supplemental Material [37], Sec. V). \mathcal{X} consistently decreases during compression showing a sudden drop at jamming for monodisperse packing, whereas for bidisperse packing is continuous. The sharp decrease in \mathcal{X} near $\hat{\phi} = 0$ in both systems suggests that density changes close to ϕ_{\max} do not result in nonaffine particle motion. Instead, the particles undergo affine displacements, indicating that the systems follow an elastic behavior. During decompression, the nonaffine motions increase again, but it is more continuous, showing fewer discontinuous jumps. Since small discontinuous changes in \mathcal{X} signal significant particle rearrangements, the absence of these discontinuities during decompression suggests that the overall packing structure at ϕ_{\max} is preserved. These findings align with the consistent \mathcal{Q}_6 values in Figs. 3 (c)-(d) across jamming and unjamming states

and with the $S(q)$ data presented in [37]. A closer examination of the configurations shows that changes in \mathcal{X} consistently coincide with reorganizations in the force chain networks. These localized particle rearrangements and their associated force chains are illustrated in Fig. 2, where the nonaffine parameter χ_i of each particle is plotted. This highlights how much a particle's displacement deviates from uniform motion near jamming and unjamming, revealing regions of local rearrangements relative to the reference configuration at ϕ_{\max} .

The nonaffine displacements are linked to the vibrational modes of the packings, especially at low ω , where a plateau appears for polycrystalline and disordered packings (see Fig. 1). Eigenvectors for $\omega = 0.05$ are extracted near jamming, at ϕ_{\max} , and near unjamming, as shown in Fig. 4. The eigenvector at ϕ_{\max} for polycrystalline monodisperse and disordered bidisperse packings displays wave-like behavior with low nonaffine motion, reflecting the macroscopic solid behavior of the system consistent with Debye's law, see Fig. 4 (b)/(e). At the plateau, the eigenvectors for jamming and unjamming reveal several localized modes with varying degrees of nonaffine displacements. This is particularly evident at jamming, where fragile regions of particles persist and may lead to rearrangements (see Fig. 4(a)/(c) for monodisperse packings and (d)/(f) for bidisperse packings). The number of particles with specific degrees of nonaffine displacements, denoted as n_{χ} , is illustrated in Fig. 2 (a)-(b) of the Supplemental Material [37]. Near the jamming and unjamming transitions, particles with low nonaffine displacements ($\chi_i < 1$) are predominant, followed by those with intermediate ($1 \leq \chi_i < 5$) and high nonaffine values ($\chi_i \geq 5$). Notably, as the system approaches unjamming, the prevalence of all nonaffine values is markedly reduced.

Gray particles in Fig. 4 represent potential rattlers ($N_c < 4$) that can provide a reference of those particles contributing to the excess of modes observed at low ω . For monodisperse packings, we find that most rattlers (approximately 10%) near jamming and unjamming exhibit low and intermediate nonaffine values, whereas few present high values, see Fig. 2 (c) in [37]. For bidisperse mixtures, small particles are those that contribute most to the nonaffine displacements at the plateau. They exhibit a quite number of particles with low nonaffine values, followed by intermediate and high ones. Only a few large particles contribute to the nonaffine displacements, see Fig. 2 (d)/(e) in [37]. Quantifying these rattler contributions during compression-decompression protocols offers insight into the nonaffine characteristics of large and small particles near jamming and unjamming, which is particularly relevant to the DOS plateau shown in Fig. 1. Even in polycrystalline systems, soft modes and rattlers near jamming and unjamming lead to deviations from the Debye law, with solid behavior restored only at high compression as the rattler fraction tends to zero, see Fig. 2 of [37]. Therefore, the DOS plateau at low ω arises primarily from the nonaffine motion of rattlers as it is pointed out in Ref. [40]. Moreover, small particles are

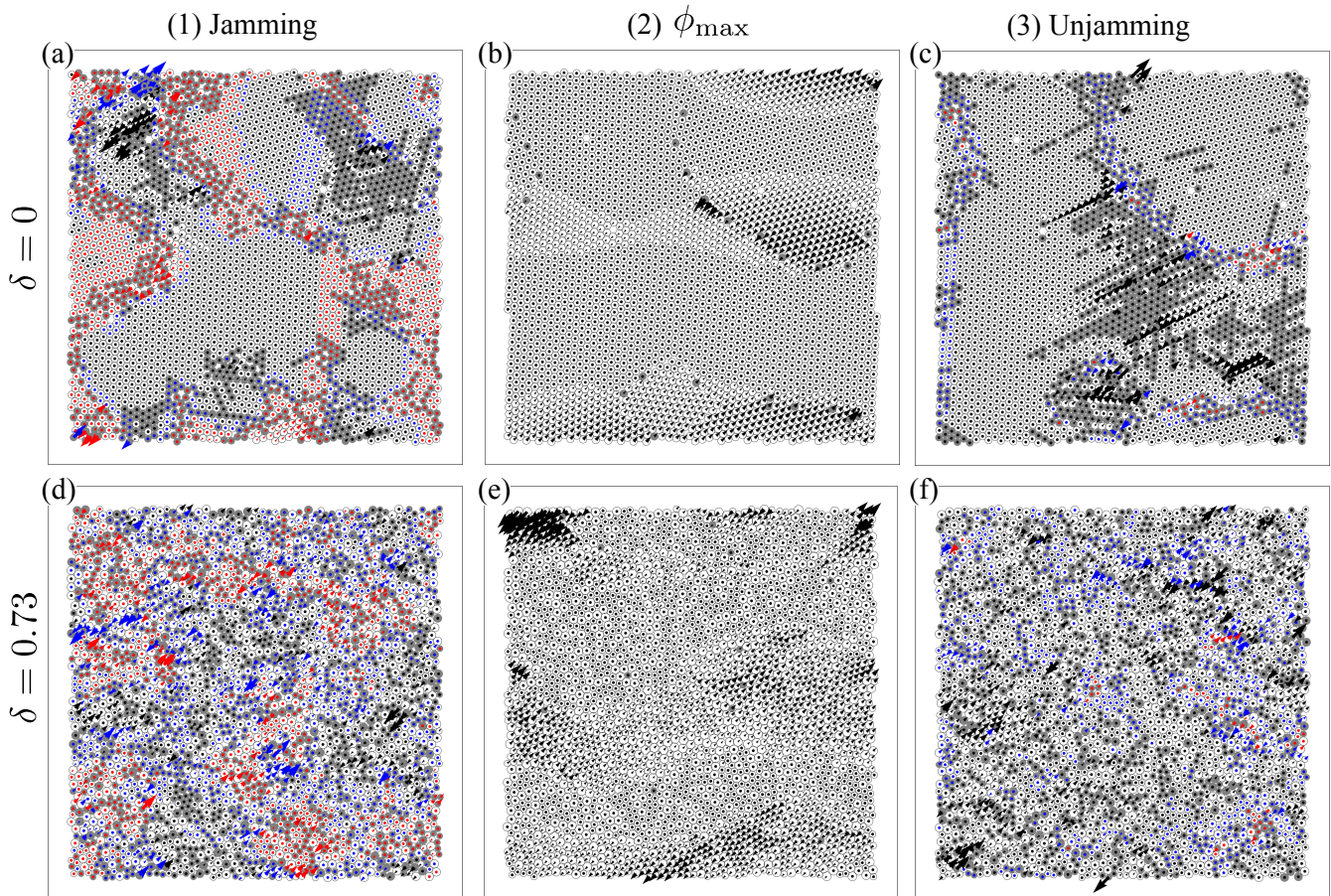


FIG. 4. Eigenvectors for $\omega = 0.05$. (Top panel) Eigenvectors of the monodisperse and (Bottom panel) bidisperse systems associated with packing fractions near jamming (1), at ϕ_{\max} (2) and near unjamming (3). The displacement fields marked with red, blue, and black arrows indicate large ($\chi \geq 5$), intermediate ($1 \leq \chi_i < 5$), and low ($\chi < 1$) nonaffine values respectively. Gray disks identify particles with less than four contacts (rattlers). Note the wave-like behavior of the particles at ϕ_{\max} consistent with the elastic nature of the system. Jamming and unjamming present localized soft modes which are responsible for the plateau observed in Fig. 1.

primarily responsible for the larger nonaffine displacements, contributing significantly to the plateau observed in the bidisperse packing.

The results presented in this study provide significant insights into the similarities in the vibrational behavior of polycrystalline and disordered granular solids during jamming and unjamming transitions. Through simulations of 2D monodisperse and bidisperse granular packings, the research demonstrates that despite differences in jamming/unjamming densities and nonaffine displacements during compression and decompression, the vibrational density of states (DOS) exhibits similar characteristics at jamming and unjamming states. Both systems exhibit a distinct low-frequency plateau, referred to as the boson peak, which correlates with soft modes, nonaffine displacements, and rattler particles. Interestingly, the study shows that while the packing structure changes during compression and decompression, the DOS

remains consistent, suggesting that mechanical behavior is preserved across jamming and unjamming transitions. This behavior highlights the elastic properties of these systems and confirms that both types of granular materials behave similarly in terms of vibrational properties at critical densities.

This work enhances our understanding of how microstructural properties influence mechanical stability and vibrational states in granular packings, providing a valuable framework for exploring polycrystalline and disordered solids under varying conditions. Future work will be to extend these findings to a broader range of size ratios and small particle concentrations, particularly regarding the first and second jamming transitions in bidisperse packings where a discontinuous transition separating jammed states dominated by large particles from those involving both large and small particles are reported [4]. Our observation that smaller particles ex-

hibit larger nonaffine displacements during the formation of stabilizing force chains provides a valuable tool for studying these transitions, which influence the stability of granular assemblies. This manuscript also presents the first evidence of a clear link between force chains and the distinct nonaffine displacements of small and large particles during jamming and unjamming states.

ACKNOWLEDGMENTS

We thank Till Kranz and Matthias Schröter, for proof-reading, fruitful discussions, and providing constructive

criticism about results and the paper. This work was supported by the German Academic Exchange Service (DAAD) under grant n° 57424730

-
- [1] T. S. Majmudar, M. Sperl, S. Luding, and R. P. Behringer, *Phys. Rev. Lett.* **98**, 058001 (2007).
- [2] C. S. O’Hern, L. E. Silbert, A. J. Liu, and S. R. Nagel, *Phys. Rev. E* **68**, 011306 (2003).
- [3] A. Donev, S. Torquato, F. H. Stillinger, and R. Connelly, *J. Appl. Phys.* **95**, 989 (2004).
- [4] J. C. Petit, N. Kumar, S. Luding, and M. Sperl, *Phys. Rev. Lett.* **125**, 215501 (2020).
- [5] N. Kumar and S. Luding, *Granul. Matter* **18**, 58 (2016).
- [6] D. Vågberg, P. Olsson, and S. Teitel, *Phys. Rev. E* **83**, 031307 (2011).
- [7] M. van Hecke, *J. Phys.: Condens. Matter* **22**, 033101 (2009).
- [8] L. E. Silbert, A. J. Liu, and S. R. Nagel, *Phys. Rev. Lett.* **95**, 098301 (2005).
- [9] C. P. Goodrich, A. J. Liu, and S. R. Nagel, *Nature Physics* **10**, 578 (2014).
- [10] L. Zhang, Y. Wang, Y. Chen, J. Shang, A. Sun, X. Sun, S. Yu, J. Zheng, Y. Wang, W. Schirmacher, and J. Zhang, *Phys. Rev. Res.* **3** (2021).
- [11] H. Tong, P. Tan, and N. Xu, *Scientific Reports* **5** (2015).
- [12] J. Amend, N. Cheng, S. Fakhouri, and B. Culley, *Soft robotics* **3**, 213 (2016).
- [13] I. Zuriguel, A. Garcimartín, D. Maza, L. A. Pugnaloni, and J. Pastor, *Phys. Rev. E* **71**, 051303 (2005).
- [14] A. Jiang, *Robotic Granular Jamming*, Ph.D. thesis, King’s College London (2014).
- [15] I. R. Peters, J. M. Amundson, R. Cassotto, M. Fahnestock, K. N. Darnell, M. Truffer, and W. W. Zhang, *Geophys. Res. Lett.* **42**, 1122 (2015).
- [16] R. Kostynick, H. Matinpour, S. Pradeep, S. Haber, A. Sauret, E. Meiburg, T. Dunne, P. Arratia, and D. Jerolmack, *Proceedings of the National Academy of Sciences* **119**, e2209109119 (2022).
- [17] E. Lawson-Keister and M. L. Manning, *Cell Biol.* **72**, 146 (2021).
- [18] L. Atia, J. J. Fredberg, N. S. Gov, and A. F. Pegoraro, *Cells & development* **168**, 203727 (2021).
- [19] L. Oswald, S. Grosser, D. M. Smith, and J. A. Käs, *J. Phys. D Appl. Phys.* **50**, 483001 (2017).
- [20] D. Forster, *Hydrodynamic fluctuations, broken symmetry, and correlation functions* (Benjamin, Reading, Massachusetts, 1975).
- [21] P. C. Martin, O. Parodi, and P. S. Pershan, *Phys. Rev. A* **6**, 2401 (1972).
- [22] J. P. Sethna, M. K. Bierbaum, K. A. Dahmen, C. P. Goodrich, J. R. Greer, L. X. Hayden, J. P. Kent-Dobias, E. D. Lee, D. B. Liarte, X. Ni, K. N. Quinn, A. Raju, D. Z. Rocklin, A. Shekhawat, and S. Zapperi, *Annu. Rev. Mater. Res.* **47**, 217 (2017).
- [23] M. Hanifpour, N. Francois, V. Robins, A. Kingston, S. Vaez Allaei, and M. Saadatfar, *Phys. Rev. E* **91**, 062202 (2015).
- [24] B. A. Klumov, Y. Jin, and H. A. Makse, *J. Phys. Chem. B* **118**, 10761 (2014).
- [25] D. Fischer, R. Stannarius, K. Tell, P. Yu, and M. Sperl, *Soft Matter* **17**, 4317 (2021).
- [26] Y. Grasselli, G. Bossis, A. Meunier, and O. Volkova, *Granul. Materials*, 71 (2017).
- [27] K. Tell, *Elastic Wave Propagation in Granular Packings*, Ph.D. thesis, Universität zu Köln (2020).
- [28] K. Tell, C. Dreißigacker, A. C. Tchapnda, P. Yu, and M. Sperl, *Rev. Sci. Instru.* **91** (2020).
- [29] J. Müller, B. Rattenbacher, K. Tell, C. Rösch, T. Welsch, M. Maurer, M. Sperl, and M. Schnellenbach-Held, *npj Microgravity* **9**, 57 (2023).
- [30] O. D’Angelo, M. Sperl, and W. T. Kranz, *arXiv preprint arXiv:2409.01297* (2024).
- [31] P. A. Cundall and O. D. Strack, *Géotechnique* **29**, 47 (1979).
- [32] T. Weinhart, L. Orefice, M. Post, M. P. van Schroyenstein Lantman, I. F. Denissen, D. R. Tunuguntla, J. Tsang, H. Cheng, M. Y. Shaheen, H. Shi, *et al.*, *Comput. Phys. Commun.* **249**, 107129 (2020).
- [33] J. C. Petit, N. Kumar, S. Luding, and M. Sperl, *Phys. Rev. E* **106**, 054903 (2022).
- [34] P. K. Morse and E. I. Corwin, *Soft Matter* **12**, 1248 (2016).
- [35] O. I. Imole, N. Kumar, V. Magnanimo, and S. Luding, *KONA Powder Part. J.* **30**, 84 (2013).
- [36] F. Göncü, O. Durán, and S. Luding, *C. R. Mécanique* **338**, 570 (2010).
- [37] See supplemental Material at ??? for details of the simulation algorithms and definitions.
- [38] J. C. Petit and M. Sperl, *Granular Matter* **25**, 43 (2023).
- [39] A. S. Clarke and H. Jónsson, *Phys. Rev. E* **47**, 3975 (1993).
- [40] R. Arévalo and M. P. Ciamarra, in *EPJ Web of Conferences*, Vol. 140 (EDP Sciences, 2017) p. 02003.

Supplementary Material:

Vibrational similarities in jamming-unjamming of polycrystalline and disordered granular packings

Juan C. Petit¹, Saswati Ganguly, and Matthias Sperl

Institut für Materialphysik im Weltraum, Deutsches Zentrum für Luft- und Raumfahrt (DLR),
51170 Köln, Germany

Institut für Theoretische Physik, Universität zu Köln, 50937 Köln, Germany

1 Technique and procedure of the simulation

We perform molecular dynamic simulations of monodisperse and bidisperse frictionless soft-disk jammed packings in 2D without gravity [1–3]. Zero gravity is employed to investigate how the DOS evolves during the development of jamming and unjamming structures, a process that is not possible to achieve under the influence of gravity. $N = 3000$ particles form the packings where their evolution is numerically solving Newton’s equation. The bidisperse packing has a number of large, N_L , and small, N_S , particles with radius r_L and r_S . The size ratio is $\delta = r_S/r_L = 0.73$ with a concentration of small particles of $X_S = N_S\delta^2/(N_L + N_S\delta^2) = 0.5$. Therefore, $\delta = 0$ represents the monodisperse packing. $\delta = 0.73$ and $X_S = 0.5$ are chosen to prevent long-range order [4–6], ensuring the emergence of local structures that reflect the real-world granular behaviors.

The linear spring-dashpot model, $\mathbf{f}_{ij}^n = f_{ij}^n \hat{\mathbf{n}} = (k_n \alpha_c + \gamma_n \dot{\alpha}_c) \hat{\mathbf{n}}$, is used for the contact between particles [1, 3, 7], where k_n is the contact spring stiffness, γ_n is the contact damping coefficient, α_c is the contact overlap and $\dot{\alpha}_c$ is the relative velocity in the normal direction $\hat{\mathbf{n}}$. A background dissipation force is imposed on each particle velocity, with constant dissipation, to damp out the kinetic energy of the particles. We use as a unit of length and time, r_L and $t = \sqrt{m_L/k}$ respectively, where m_L is the mass of the large particles and k is the stiffness constant.

The initial configuration of the packing is such that disks are uniformly generated at random in a 2D box with uniform random velocities and with an initial packing fraction of $\phi_{\text{ini}} = 0.3$. Large overlaps lead to an initial peak in kinetic energy, but this is quickly damped by the background medium and collisions. Low-density systems with high kinetic energy contribute to the rapid randomization of particles. The granular gas is then isotropically compressed to approach an initial direction-independent configuration with the target packing fraction ϕ_0 below the jamming density at ϕ_J , see Ref. [3] for further details. The system then undergoes a relaxation process to eliminate any remaining kinetic energy. Once relaxation is complete, isotropic compression begins and continues until the packing fraction reaches the maximum value, $\phi_{\text{max}} = 0.95$. Then, the isotropic decompression process proceeds at the same rate as the compression until ϕ_0 is reached again. The mean volumetric strain rate, $\dot{\epsilon}_v$, during the compression-decompression process in this study is approximately one hundred times greater than in previous work [8], reaching values around $\dot{\epsilon}_v \sim 10^{-4}$. Despite this accelerated rate, the protocol successfully generates polycrystalline monodisperse and disordered bidisperse packings. Moreover, the protocol maintains a stable energy ratio—kinetic to potential energy—of approximately 10^{-4} near the jamming and unjamming transitions, ensuring that the packings remain in mechanical equilibrium throughout the process.

2 Density of states (DOS)

We present the density of states (DOS) throughout the compression-decompression process, with a focus on the DOS near jamming and unjamming. This comparison emphasizes the vibrational behavior of polycrystalline monodisperse and disordered bidisperse packings in relation to the structural features discussed earlier.

¹Juan.Petit@dlr.de

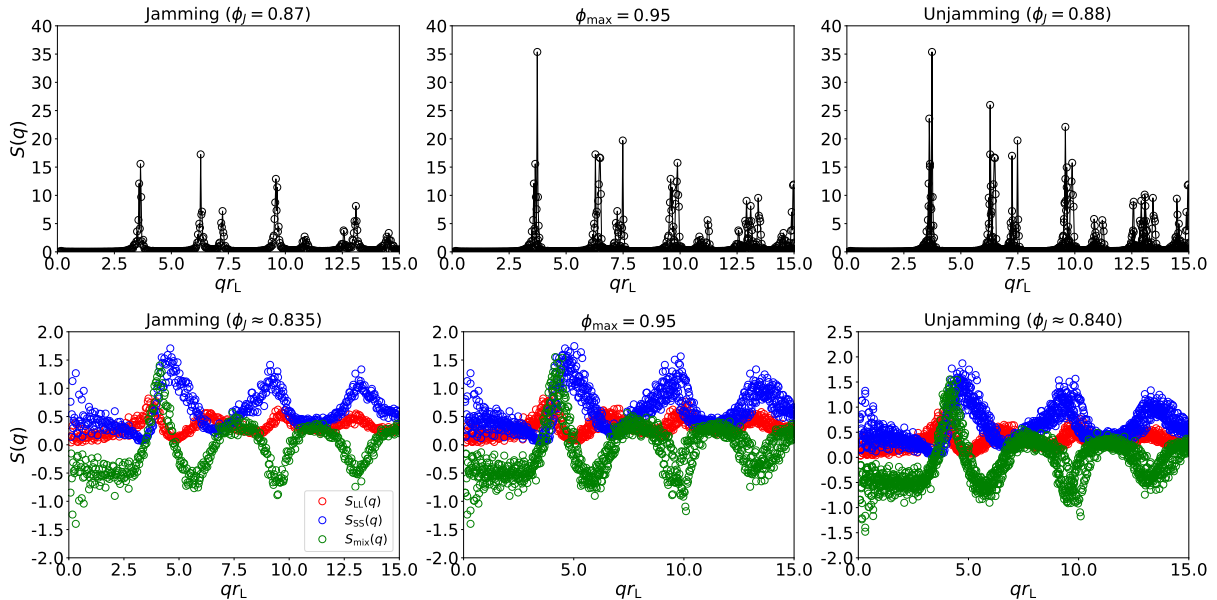


Figure 1: The structure factor, $S(q)$, is shown for both monodisperse (top) and bidisperse packings (bottom) across three states: near jamming, at maximum packing density ϕ_{\max} , and near unjamming. Notably, minimal changes are observed in the packing structure across these states, indicating a consistent organization of particles despite variations in packing density.

The DOS is calculated by diagonalizing the dynamical matrix, \mathbf{D} , where the obtained eigenvalues are related to the frequencies of the system and the eigenvectors with the vibrational modes of the particles. Off-diagonal elements of \mathbf{D} from different particles $i \neq j$ are calculated by

$$D_{ij} = -k \frac{\vec{r}_{ij} \otimes \vec{r}_{ij}}{r_{ij}^2} + \frac{f_{ij}}{r_{ij}} \left(I - \frac{\vec{r}_{ij} \otimes \vec{r}_{ij}}{r_{ij}^2} \right), \quad (1)$$

where \vec{r}_{ij} and f_{ij} are the distance vector and force magnitude between particle i and j , respectively. I denotes the unit tensor. The diagonal elements from same particle $i = j$ are determined by $D_{ii} = -\sum_{j \in \Gamma_i} D_{ij}$, where Γ_i specifies the number of j particles in contact with particle i . We have also considered that the particle mass is one, see Ref. [9].

3 Structure factor quantification

We calculate the partial structure factors, $S(q)$, at jamming, at ϕ_{\max} , and at unjamming. This analysis enables us to investigate the structural contributions and structural changes associated with each configuration type (in the case of bidisperse packings) within both jammed and unjammed states. A general definition of the partial $S(q)$ is

$$\begin{aligned} S_{\nu\beta}(q) &= \frac{1}{N} \sum_{i=1}^{N_\nu} \sum_{j=1}^{N_\beta} \cos(\mathbf{q} \cdot \mathbf{r}_\nu^i) \cos(\mathbf{q} \cdot \mathbf{r}_\beta^j) \\ &+ \frac{1}{N} \sum_{i=1}^{N_\nu} \sum_{j=1}^{N_\beta} \sin(\mathbf{q} \cdot \mathbf{r}_\nu^i) \sin(\mathbf{q} \cdot \mathbf{r}_\beta^j) \end{aligned} \quad (2)$$

where $\nu\beta \in \{L, S\}$ and the sum runs over all ν and β particles. Thus, the total structure factor $S(q)$ can be decomposed into contributions: $S_{LL}(q)$, $S_{SS}(q)$, $S_{LS}(q)$, and $S_{SL}(q)$. By symmetry, we have $S_{LS}(q) = S_{SL}(q)$. For simplicity, we label this shared term as $S_{\text{mix}}(q)$, where ‘‘mix’’ emphasizes the equivalence between $S_{LS}(q)$ and $S_{SL}(q)$. Therefore, the total structure factor can be expressed as $S(q) = S_{LL}(q) + S_{SS}(q) + 2S_{\text{mix}}(q)$. In monodisperse packings, $S(q) = S_{LL}(q)$ is only calculated. Fig. 1

illustrates the structure factors for both monodisperse and bidisperse packings near jamming, at ϕ_{\max} , and near unjamming. At jamming, we observe multiple peaks in $S(q)$ for the monodisperse packing, reflecting its polycrystalline nature. In contrast, the bidisperse mixture exhibits a partial $S(q)$ with broader peaks, indicative of a disordered structure with local ordering. We interpret this as a result of the bidisperse packing being locally ordered but globally disordered. Further compression increases the density of both systems, as seen in the development of new peaks and the growth of existing peaks, particularly at ϕ_{\max} in both monodisperse and bidisperse packings. Upon decompression, only minimal structural changes arise from particle rearrangements, yet the jamming and unjamming states retain similar structural features. This suggests that they are structurally comparable, although the unjamming state may exhibit slightly higher local particle densities.

4 Definition of the contact orientational order (COR), \mathcal{Q}_6 .

To understand the evolution of the packing structure, we calculate the contact orientational order (COR) defined as $\mathcal{Q}_6 = \frac{1}{N} \sum_{j=1}^N \mathcal{Q}_{6j}$ where $\mathcal{Q}_{6j} = \left| \frac{1}{N_c^j} \sum_{k=1}^{N_c^j} e^{6i\theta_{kj}} \right|$, which quantifies the formation of potential six-fold lattice structures within the packing. Here, N_c^j represents the number of contacts for the j th particle, and θ_{kj} is the contact angle between particles k and j , measured with respect to the x-axis. This approach, introduced in Ref. [10], avoids neighborhood ambiguities inherent in the bond orientational order (BOR) metric, see Refs. [11–17], and is sensitive to sudden changes in contact number or other structural features. Rather than using a separate detection method to identify nearest neighbors, COR is defined directly by particle contacts. This means that, for each particle i , its neighbors are implicitly defined by contact. According to the definition of \mathcal{Q}_6 , in the absence of a jammed structure (i.e., before jamming), \mathcal{Q}_6 should ideally be zero. However, isolated clusters of contacting particles may yield low, nonzero \mathcal{Q}_6 values. Unlike prior definitions where local bond orientational order in highly amorphous packings is expected to vanish at jamming, COR allows for a finite, low \mathcal{Q}_6 value at the onset of jamming in amorphous packings. On the other hand, high values of \mathcal{Q}_6 , particularly those close to one, indicate an ordered hexagonal packing structure. Notably, for dense packings where $\phi \gg \phi_J$, we expect BOR and COR converge, as BOR’s detection method will naturally identify those particles in contact with particle i as its nearest neighbors. Figs. 3 (c)-(d) in the paper shows the evolution of \mathcal{Q}_6 as a function of packing fraction.

5 Cumulative nonaffine displacements (χ)

The nonaffine parameter χ provides a geometric measure of local structural deviations from homogeneous, system-wide deformations due to applied volume or shear strains. Defined over a chosen coarse-graining neighborhood volume Ω around a particle, the nonaffine parameter χ and the best-fit affine strain ϵ are given by

$$\chi = \Delta P \Delta, \text{ with } P = I - RQ, \quad (3)$$

$$\epsilon = Q \Delta, \text{ where } Q = (R^T R)^{-1} R^T. \quad (4)$$

Here, χ and ϵ are projections of the displacement fields Δ using the projector P , based on a reference configuration R [18]. To compute χ for each particle in an N -particle configuration, the displacement fields Δ within the neighborhood Ω are compared to the reference relative positions R . For defect-free crystalline systems under deformation or thermal fluctuations, R is typically chosen as the zero-temperature energy minimum configuration. For polycrystalline monodisperse or disordered bidisperse packings, we use the configuration at ϕ_{\max} as the reference, leveraging its mechanical stability to analyze microstructural changes during jamming and unjamming in granular assemblies. The parameter χ , with units of $(\text{length})^2$, can be derived from the eigenvalues of the matrix PCP , which itself is projected from the covariance matrix $C = \langle \Delta^T \Delta \rangle$ [18]. Prior work (e.g., Refs. [19–22]) demonstrates that the eigenvectors of PCP correspond to thermally induced local nonaffine modes related to defect precursors in crystalline materials in both two and three dimensions. In disordered systems,

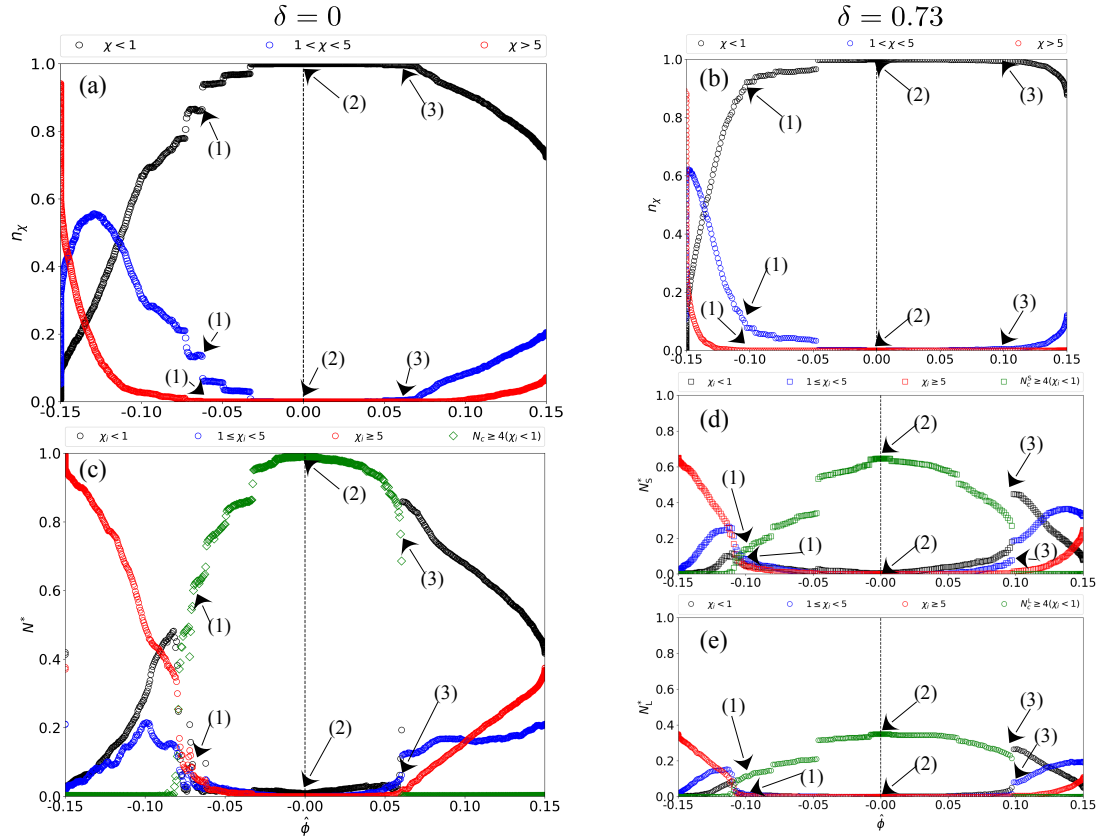


Figure 2: (a)-(b) Particle fraction, n_χ , classified by nonaffine displacement levels—low ($\chi_i < 1$), intermediate ($1 \leq \chi_i < 5$), and high ($\chi_i \geq 5$)—as a function of relative packing fraction, $\hat{\phi}$, for monodisperse and bidisperse packings. (c)-(d) Fraction of rattler particles ($N_c < 3$) showing distinct nonaffine values, consistent with (a) and (b). Additionally, the fraction of non-rattlers ($N_c \geq 4$) with $\chi_i < 1$ is included to indicate predominantly affine displacements. In the bidisperse mixtures, rattlers are further divided into large and small particles, as shown in (d) and (e). Arrows in the plots mark key states: near jamming (1), maximum packing fraction ϕ_{\max} (2), and near unjamming (3), aligning with the states presented in Fig. 1 of the paper. Note that the numbered arrows are repeated to indicate the state at various nonaffine displacements.

χ is associated with shear transformation zones or soft spots, areas with a heightened tendency for irreversible particle rearrangements [23–25]. As a 2D granular medium with N particles undergoes jamming and unjamming with varying packing fraction ϕ at a finite strain rate $\dot{\epsilon}_v$, we track the cumulative nonaffine displacements, $\mathcal{X} = \sum_{i=1}^N \chi_i$, where χ_i denotes the nonaffine displacement of the i th particle. Figs. 3 (e)-(f) in the paper illustrate the evolution of \mathcal{X} as a function of $\hat{\phi}$ for monodisperse and bidisperse packings.

6 Nonaffine and rattler particle fraction

To gain insight into the packing structure, we examine the evolution of the particle fraction, n_χ , corresponding to low ($\chi_i < 1$), intermediate ($1 \leq \chi_i < 5$), and high ($\chi_i \geq 5$) nonaffine displacements throughout the compression-decompression protocol. This analysis is presented in Fig. 1 (a)-(b) for both monodisperse and bidisperse packings. As jamming is approached, particles with intermediate and high nonaffine values decrease, while those with low nonaffine values increase. At the jamming density (indicated by arrow (1)), low nonaffine displacements dominate, with intermediate and high values present in diminishing quantities. The corresponding packing configurations and nonaffine displacements are illustrated in Fig. 4(a)/(d) of the paper. Upon further compression, the system becomes

denser, resulting in low nonaffine displacements dominating the packing structure, as shown in Fig. 4 (b)/(e) at the maximum packing fraction, ϕ_{\max} . In this densely packed state, particle displacements are predominantly affine. During decompression, particles with low nonaffine displacements reduce, while intermediate and high nonaffine values experience a slight increase. At unjamming (arrow (3)), the system exhibits fewer particles with nonaffine displacements compared to the jamming state, as shown in Fig. 4 (c)/(f). This observation suggests that the packing structure undergoes minimal evolution from ϕ_{\max} to unjamming.

We further analyze the evolution of the number of rattlers ($N_c < 4$) exhibiting various degrees of nonaffine displacement, as shown in Fig. 2 (a)-(b). Rattlers are shown as gray disks in Fig. 4 of the paper. As jamming is approached, the number of rattlers (N^*) with high nonaffine values decreases, while those with low and intermediate nonaffine values increase, as depicted in Fig. 2 (c)-(e). At the jamming transition (arrow (1)), the proportion of rattlers exhibiting nonaffine displacements drops by approximately 10% for both monodisperse and bidisperse packings. Meanwhile, non-rattlers ($N_c \geq 4$) with low nonaffine displacements become dominant. Intermediate and high nonaffine values among non-rattlers are omitted here, as they approach zero, reflecting the tendency of particles with $N_c \geq 4$ to exhibit primarily affine displacements. At maximum packing density, ϕ_{\max} (arrow (2)), the number of rattlers reduces to zero, while non-rattlers reach their peak, confirming the predominance of affine displacements in this dense state. As unjamming approaches (arrow (3)), rattlers begin to reappear with nonaffine displacements, with around 10% of them showing low and intermediate nonaffine values in the monodisperse case and among smaller particles in the bidisperse packing, as illustrated in Fig. 2 (c)/(d). Only a few large particles contribute to nonaffine displacements, as seen in Fig. 2 (e) and qualitatively in Fig. 4 of the paper. These observations imply that the density of states (DOS) plateau at low frequencies (ω) arises largely from the nonaffine motion of rattlers. In particular, small particles play a critical role in generating these nonaffine displacements, contributing significantly to the plateau observed in the bidisperse packing.

References

- [1] Peter A. Cundall and Otto D.L. Strack. *Géotechnique*, 29(1):47–65, 1979.
- [2] Thomas Weinhart, Luca Orefice, Mitchel Post, Marnix P. van Schrojenstein Lantman, Irana F.C. Denissen, Deepak R. Tunuguntla, J.M.F. Tsang, Hongyang Cheng, Mohamad Yousef Shaheen, Hao Shi, et al. *Compu. Phys. Commun.*, 249:107129, 2020.
- [3] Juan C. Petit, Nishant Kumar, Stefan Luding, and Matthias Sperl. *Phys. Rev. E*, 106(5):054903, 2022.
- [4] T. S. Majmudar, M. Sperl, S. Luding, and R. P. Behringer. *Phys. Rev. Lett.*, 98:058001, 2007.
- [5] C. S. O’Hern, L. E. Silbert, A. J. Liu, and S. R. Nagel. *Phys. Rev. E*, 68:011306, 2003.
- [6] Peter K. Morse and Eric I. Corwin. *Soft Matter*, 12(4):1248–1255, 2016.
- [7] Stefan Luding. *Granul. Matter*, 10:235–246, 2008.
- [8] Nishant Kumar and Stefan Luding. *Granul. Matter*, 18(3):58, 2016.
- [9] Yusuke Hara, Hideyuki Mizuno, and Atsushi Ikeda. *arXiv preprint arXiv:2311.09509*, 2023.
- [10] Juan C. Petit and Matthias Sperl. *Granul. Matter*, 25(3):43, 2023.
- [11] Paul J. Steinhardt, David R. Nelson, and Marco Ronchetti. *Phys. Rev. B*, 28(2):784, 1983.
- [12] C.L. Martin and R.K. Bordia. *Phys. Rev. E*, 77(3):031307, 2008.
- [13] Nathan Duff and Daniel J. Lacks. *Phys. Rev. E*, 75(3):031501, 2007.
- [14] Steven Fortune. *Computing in Euclidean geometry*, pages 225–265, 1995.

- [15] Anuraag R. Kansal, Salvatore Torquato, and Frank H. Stillinger. *Phys. Rev. E*, 66(4):041109, 2002.
- [16] Walter Mickel, Sebastian C. Kapfer, Gerd E. Schröder-Turk, and Klaus Mecke. *Chem. Phys.*, 138(4):044501, 2013.
- [17] Jan Haeberle, Matthias Sperl, and Philip Born. *Eur. Phys. J. E*, 42(11):1–7, 2019.
- [18] Saswati Ganguly, Surajit Sengupta, Peter Sollich, and Madan Rao. *Phys. Rev. E*, 87:042801, 2013.
- [19] Saswati Ganguly, Surajit Sengupta, and Peter Sollich. *Soft Matter*, 11:4517–4526, 2015.
- [20] Saswati Ganguly, Priti S. Mohanty, Peter Schurtenberger, Surajit Sengupta, and Anand Yethiraj. *Soft Matter*, (13):4689, 2017.
- [21] Pankaj Popli, Sayantani Kayal, Peter Sollich, and Surajit Sengupta. *Phys. Rev. E*, 100:033002, Sep 2019.
- [22] Amartya Mitra, Saswati Ganguly, Surajit Sengupta, and Peter Sollich. *J. Stat. Mech. Theory Exp.*, 2015(6):P06025, 2015.
- [23] M. L. Falk and J. S. Langer. *Phys. Rev. E*, 57:7192–7205, Jun 1998.
- [24] B. A. DiDonna and T. C. Lubensky. *Phys. Rev. E*, 72:066619, Dec 2005.
- [25] R. Milkus and A. Zaccone. *Phys. Rev. B*, 93:094204, Mar 2016.